Journal of Materials Chemistry A

Accepted Manuscript

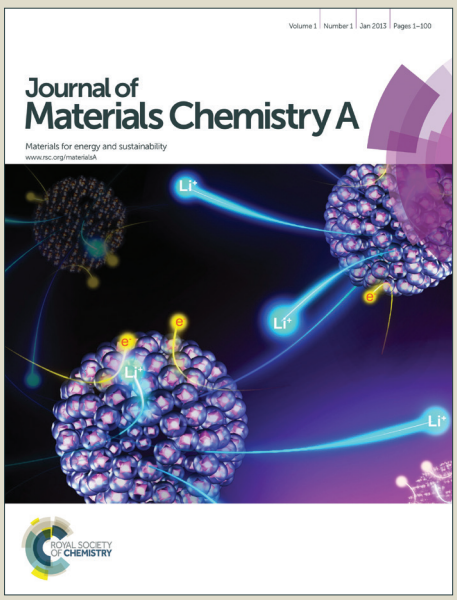

ROYAL SOCIETY OF CHEMISTRY

www.rsc.org/materialsA

Journal of Materials Chemistry A

Paper

A Nanostructured Chromium (III) Oxide/ Tungsten (VI) Oxide p-n Junction Photoanode toward Enhanced Efficiency for Water Oxidation

Received 00th January 20xx,
Accepted 00th January 20xx

DOI: 10.1039/x0xx00000x

www.rsc.org/

Zhuofeng Hu,[b] Mingkun Xu,[a] Zhurui Shen,[ab*] Jimmy C. Yu[*b]

A nanostructured chromium(III) oxide/ tungsten(VI) oxide (Cr_2O_3/WO_3) p-n junction photoanode is established here. It is prepared by depositing Cr_2O_3 nanoparticles on to WO_3 nanosheet array. The formation of p-n junction is confirmed by Mott-Schottky plot and photocurrent measurement. Electrochemical and spectroscopic methods indicate that the recombination rate of photogenerated charges becomes lower in this photoanode. Consequently, its onset potential shifts negatively by about 0.1 V and photocurrent density increases from 0.7 to 1.8 mA cm^{-2} at 1.8 V vs. RHE. The incident photon-to-current efficiency (IPCE) also shows a one-fold improvement. In addition, the construction of p-n junction leads to an increase of faradaic efficiency (holes to oxygen) from 73.9% to 92.0%, which is attributed to the suppression of side reactions in the water oxidation. This work will bring new inspirations for improving the performance of WO_3 and other photoanodes.

Introduction

Metal oxide semiconductors are often used to convert solar energy into electricity and chemical fuels in photoelectrochemical cells (PECs).[1-7] With a band gap of 2.7 eV, WO_3 can utilize the solar spectrum up to ~460 nm.[8-11] Moreover, its positive valence band edge (3.0 eV vs. RHE) is sufficient to overcome the overpotential of water oxidation.[12, 13] Therefore, WO_3 has been widely studied as a promising photoanode in photoeletrochemical water oxidation.[8-22]

The performance of WO_3 photoanodes mainly depends on the separation efficiency of photogenerated electron/hole pairs.[1, 23] So far, several routes have been developed for the improvement: (i) deposition of water oxidation cocatalyst;[24, 25] (ii) introduction of hole sacrifice agents[23, 26]; (iii) doping heteroatoms into the lattice [27, 28] and (iv) shortening the diffusion-length of photogenerated charges.[29]

Apart from the aforementioned methods, building a nanostructured p-n junction photoanode is a promising approach to reduce the charge recombination. The p-n junction can facilitate the charge separation by the internal electric field in its depletion region.[30-33] For example, n-type $BiVO_4$ exhibited lower charge recombination rate at the surface trapping states when loaded with p-type NiO.[34] N-type TaON/p-type Cu_2O showed a maximum IPCE of 59% at a wavelength of 400 nm, and reached 3.06 mA cm^{-2} under AM 1.5G simulated sunlight at 1.0 V vs. RHE.[35] However, there are few reports about the enhancement of WO_3 photoanode by constructing a p-n junction.

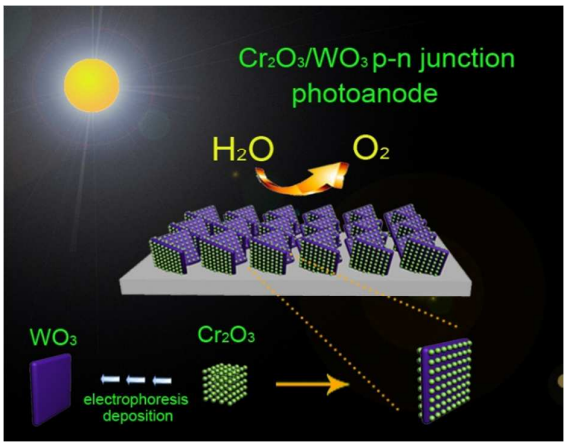

Scheme 1 A diagram of the nanostructured Cr_2O_3/WO_3 p-n junction photoanode toward high faradaic efficiency in water oxidation.

Cr_2O_3, an p-type semiconductor with a bandgap of 3.4 eV,[36, 37] has been extensively studied in the fields of heterogeneous catalysis,[38] photocatalysis[36] and hydrogen absorption.[39] Herein, we use nanostructured Cr_2O_3/WO_3 p-n junction as an example to suppress the charge recombination in water oxidation. P-type Cr_2O_3 nanocrystals are decorated on the surface of n-type WO_3 nanosheets by electrophoresis. Characterization by SEM, TEM and XRD etc. show that the two types of materials contact intimately with each

[a] Key Laboratory of Advanced Ceramics and Machining Technology, Ministry of Education, School of Materials Science and Engineering, Tianjin University, Tianjin 300072, PR China, E-mail:shenzhurui@tju.edu.cn
[b] Department of Chemistry, The Chinese University of Hong Kong, Shatin, New Territories, Hong Kong, China & Shenzhen Research Institute, The Chinese University of Hong Kong, Shenzhen, PR China , E-mail:jimyu@cuhk.edu.hk
Electronic Supplementary Information (ESI) available: [It consists of additional SEM, TEM, EDX, optical image, electrochemical data and gas evolution data etc.]. See DOI: 10.1039/x0xx00000x

other. Results from photoelectrochemical measurements confirm that the as-prepared Cr_2O_3/WO_3 photoanode exhibits higher photocurrent density and incident photon-to-current efficiency (IPCE) than those of WO_3 photoanode. Besides, the faradaic efficiency for water oxidation is increased from 73.9% (WO_3 photoanode) to 92.0% (Cr_2O_3/WO_3 photoanode). Based on the electrochemical and spectroscopic measurements, a possible mechanism is proposed to explain the superior performance of the Cr_2O_3/WO_3 photoanode.

Experimental Section

All chemical reagents are commercially available and used as received.

Preparation of WO_3 nanosheets on FTO glasses (WO_3 electrode). 70 mg of sodium tungsten (Na_2WO_4) was firstly dissolved in 10 mL of deionized (DI) water. Then, 5 mL of 10 M hydrochloric acid (HCl) was added dropwise. Once the solution became light yellow, 70 mg of ammonium oxalate ($(NH_4)_2C_2O_4$) was added. After 10 minutes of stirring, the solution was transferred into a 20 mL Teflon-lined stainless steel autoclave. A FTO glass substrate was cleaned ultrasonically in ethanol and acetone, and was placed into the autoclave, sealed and heated at 120 °C for 12 hours. Thereafter, the FTO glass was taken out and washed with ethanol and water. A film of yellow $WO_3 \cdot H_2O$ can be observed on the surface of the FTO glass. The film was then calcination at 550 ^oC for 3 hours to transform $WO_3 \cdot H_2O$ into WO_3 and improve the contact to FTO.

Preparation of Cr_2O_3 nanocrystals. 340 mg of sodium dichromate ($Na_2Cr_2O_7$) was firstly dissolved in 19 mL of DI water. Then, 1 mL of 6M HCl was added dropwise. The mixed solution was transferred into a 20 mL Teflon-lined stainless steel autoclave, sealed and heated at 180 °C for 12 hours. The product was collected by centrifugation and dried at 80 ^oC overnight. Finally, the product was calcination at 550 ^oC for 3 hours to improve its crystallinity.

Deposition of Cr_2O_3 nanocrystals on WO_3 electrode. The Cr_2O_3 nanocrystals were deposited onto the WO_3 electrode by electrophoretic method. 5 mg of the Cr_2O_3 nanocrystals was dispersed in 25 mL acetone solution of iodine (5 mg, making the particles positive charged). A WO_3 electrode and an auxiliary FTO glass were fixed in parallel with a distance of 1 cm. The bottom parts of the FTO glasses (1.5×1.5 cm^2) were immersed into the suspension. Then 20 V of dc voltage was applied between the two electrodes for 10, 25 and 85 seconds. The yellow WO_3-FTO electrode became light green after the deposition.

Materials Characterization. Scanning electron microscopy (SEM) observations were carried out using the Hitachi Model S-4800, FEI Quanta 400 and (JEOL) JSM–7500F microscopes. The (JEOL) JSM–7500F microscope is coupled with an energy dispersive X-ray (EDX) spectrometer (Oxford Instrument). Transmission electron microscopy (TEM) was conducted with a CM-120 microscope (Philips, 120 kV) coupled with an energy-dispersive X-ray (EDS) spectrometer (Oxford Instrument). X-ray diffraction (XRD) patterns were collected on a Rigaku SmartLab X-ray diffractometer using a Cu Kα source irradiation (λ=1.5406 Å). X-Ray photoelectron spectroscopy (XPS) analysis was performed using a Sengyang SKL-12 spectrometer equipped with a VG CLAM 4 MCD electron energy analyzer and twin anode Mg Kα radiation (1253.6 eV) or Al Kα radiation (1496.3 eV) X-ray sources.

Photoelectrochemical measurements. WO_3 and Cr_2O_3/WO_3 electrodes were fixed into the photoanodes by securing a copper wire onto a bare portion of the substrates via silver paste. All the photoelectrochemical measurements were performed in a three-electrode cell with a saturated-potassium-chloride silver chloride electrode (Ag/AgCl) as a reference electrode, a platinum foil (1.0×1.0 cm^2) as a counter electrode, and the WO_3 and Cr_2O_3/WO_3 photoanodes as the working electrodes. The electrolyte was 0.1M Na_2SO_4. Linear sweeps and transient photocurrent were measured by a CHI 660D electrochemical workstation. The lifetime of electron was measured by plotting the Bode phase at open-circuit voltage. A 300 W Xenon arc lamp coupled with an Air Mass (AM) 1.5 global filter (100 mW cm^{-2}) were used as the light source. The AM 1.5 global filter corrects the output of a Xenon lamp to better match the solar spectrum with a 37 degree tilt angle. A series of band-pass light filters were also equipped onto the Xenon arc lamp for IPCE measurements.

Gases evolution measurements. The gases (oxygen/hydrogen) evolution by photoelectrochemical water splitting was conducted in the airtight H-type reactor connected to a closed gas circulation system. The experiment was carried out at 1.0 V vs. RHE in 0.1 M Na_2SO_4 electrolyte under the illumination of a 300 W Xenon arc lamp. The yield of oxygen and hydrogen was measured by a gas chromatography equipped with a TCD detector.

Results and Discussion

In a typical synthesis, the WO_3 nanosheets were prepared on a FTO conducting glass. Fig. 1a shows that the size of WO_3 nanosheets is c.a. 1 um, and the thickness is c.a. 200 nm. Its XRD pattern (Fig. 2) is well indexed with the standard card of monoclinic phase WO_3 (JCPDS No. 43-1035). The Cr_2O_3 nanocrystals have a uniform size of c.a. 20-40 nm with a rhombohedra crystalline phase (ESI, Fig. S1, XRD see Fig. 2, JCPDS No. 38-1479). Then, the Cr_2O_3 nanocrystals were deposited on the surface of WO_3 nanosheets by an electrophoresis method.[40] After 10 s of deposition, the WO_3 nanosheets were homogeneously covered by Cr_2O_3 nanocrystals (Fig. 1b, c). The HRSEM images show that the Cr_2O_3 nanocrystals can locate at the top/lateral faces of WO_3 nanosheets, and they contact well with each other (Fig. 1c, d). The XRD pattern of Cr_2O_3/WO_3 displays the peaks of both monoclinic WO_3 and rhombohedra Cr_2O_3, which further confirms the formation of their heterostructure (Fig. 2). The EDX (SEM) results show that the molar ratio of Cr: W is approx. 0.70 after 10 s of deposition (average value from 5 sites, Table S1). TEM analysis is then performed here to further study its microstructure (Fig. 1e, f; the low resolution image and EDX see ESI, Fig. S2). As shown in Fig. 1e, a Cr_2O_3

nanocrystal contacts intimately with a WO_3 nanosheet. From its enlarged image, the clear lattice fringes with *d*-spacing of 0.36 nm and 0.26 nm can be ascribed to the (012) facets of Cr_2O_3 and (202) facets of WO_3, respectively (Fig. 1f). This result directly evidences their close interface contact, which will promote the charge separation in the PECs.

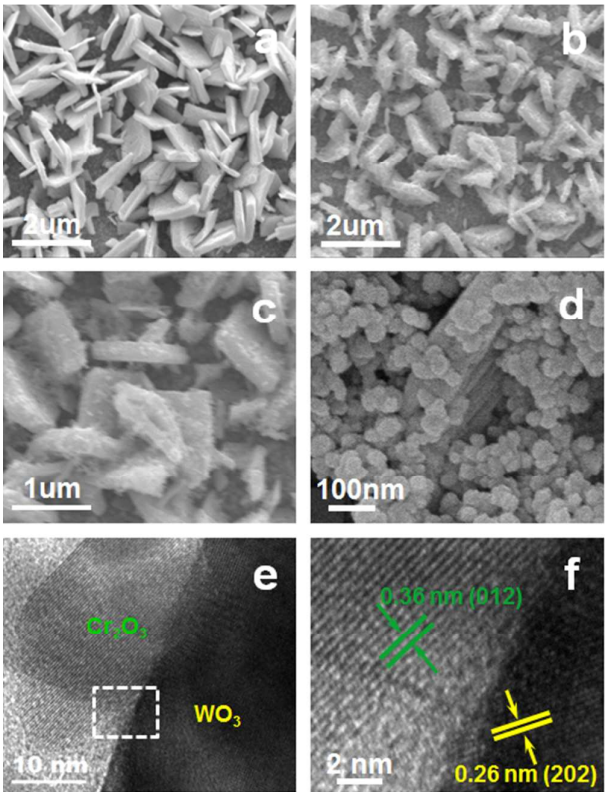

Fig. 1 SEM images of (a) WO_3 on FTO, (b-d) Cr_2O_3/WO_3 on FTO after 10 s of electrophoresis deposition and its HRTEM images (e, f).

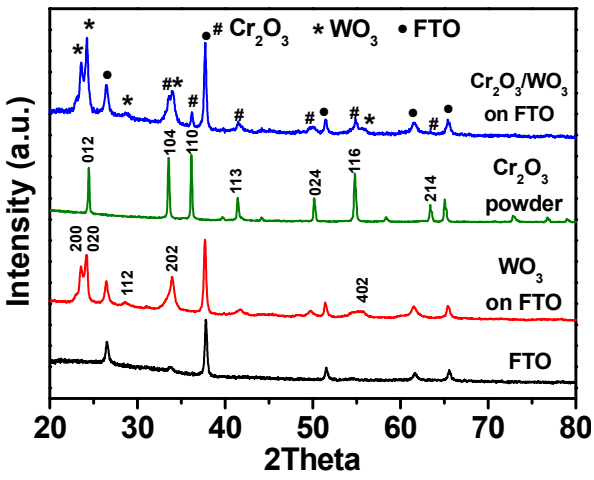

Fig. 2 XRD patterns of FTO glass, WO_3 on FTO, Cr_2O_3 powder and Cr_2O_3/WO_3 on FTO after 10 s of electrophoresis deposition.

To further study the chemical nature of Cr_2O_3/WO_3 heterostructure, its XPS spectra were recorded (ESI, Fig. S3). The W 4f spectrum of Cr_2O_3/WO_3 shows two peaks at 35.2 eV and 37.4 eV, indicating the presence of W^{6+} [41, 42] (ESI, Fig. S3a). This is consistent with that of WO_3 nanosheets, which suggests that the WO_3 kept stable during the electrophoresis process (ESI, Fig. S3b). Its O 1s spectrum can be deconvoluted into two main components after Gaussian fitting:[43, 44] One is 530. 3 eV (O_L), corresponding to the O^{2-} ions in the WO_3 and Cr_2O_3 lattices. The other is 531. 8 eV (O_v), indexing to the O^{2-} ions in the oxygen-deficient regions (ESI, Fig. S3c). Compared with the O 1s spectrum of WO_3 nanosheets, the relative quantity of O_v peak in Cr_2O_3/WO_3 is larger, which can be ascribed to more defect regions in Cr_2O_3 nanocrystals.

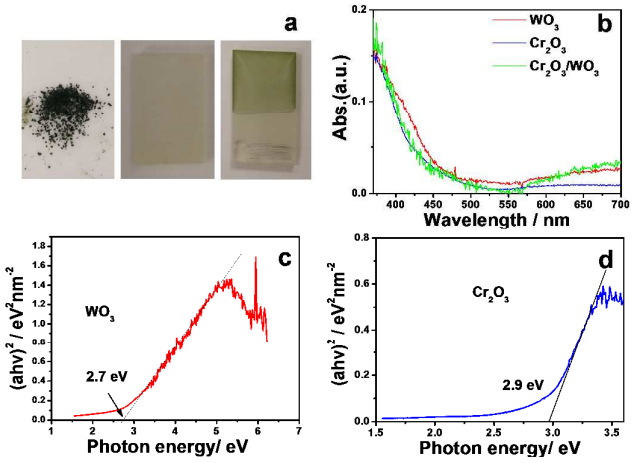

Fig. 3 (a) Optical images of Cr_2O_3 powder, WO_3 on FTO and Cr_2O_3/WO_3 on FTO after 10 s of electrophoresis deposition (left to right), (b) UV-vis diffuse reflectance spectra of WO_3 on FTO, Cr_2O_3 powder and Cr_2O_3/WO_3 on FTO after 10 s of electrophoresis deposition, (c, d) band gaps calculated from Kubelka–Munk plots of WO_3 on FTO and Cr_2O_3 powder.

The as-prepared WO_3 nanosheets on FTO exhibit a light yellow color (Fig. 3a). This is consistent with its UV-vis diffuse reflectance spectrum with an absorption edge at c.a. 460 nm (Fig. 3b). The band gap of WO_3 naonsheets is estimated to be c.a. 2.7 eV from the linear approximation in the Kubelka–Munk plot[45] (Fig. 3c). Cr_2O_3 nanocrystals show a light green color (Fig. 3a). Its absorption edge is at c.a. 430 nm, corresponding to a band gap of 2.9 eV (Fig. 3b, d). This value is smaller than that of its bulk counterpart (3.5 eV),[36] which can be ascribed to the quantum confinement effect.[46] The Cr_2O_3/WO_3 on FTO also displays a pale green color due to the coating of Cr_2O_3 nanocrystals (Fig. 3a). Its UV-vis diffuse reflectance spectrum exhibits the characteristic of both Cr_2O_3 and WO_3.

PEC measurements were conducted in a three-electrode electrochemical cell in 0.1 M Na_2SO_4 solution (pH: c.a. 7.0). The Linear sweep voltammograms were recorded under the irradiation of a 100 mW cm^{-2} simulated sunlight in the potential range of 0.8 to 2.2 V vs. RHE, as shown in Fig. 4a (their dark currents see ESI, Fig. S4). The photocurrent density (J) of WO_3 begins to rise at 1.0 V vs.

RHE and reaches about 0.7 mA cm^{-2} at 1.8 V vs. RHE. The onset potential is 0.45 V positive than its flat band potential (Fig. 4a) due to poor charge transfer at the interface induced by slow water oxidation kinetic.[10, 47, 48] After 10 s electrophoresis deposition of Cr_2O_3 nanocrystals, the saturated photocurrent increases from 0.7 to 1.8 mA cm^{-2} (Fig. 4a). This suggests the charge separation in the photoanode is greatly enhanced. However, with longer electrophoresis duration, excessive amounts of Cr_2O_3 nanocrystals will be deposited (ESI, Fig. S5, Fig. S6), and they will block light and decrease the photocurrent density (Fig. 4a, ESI, Fig. S5). Different from the saturated photocurrent density, the onset potentials are stable at 0.9 V vs. RHE for all the Cr_2O_3/WO_3 photoanodes (Fig. 4a). This is 0.1 V lower than that of bare WO_3 photoanode. In addition, we also conducted the calcination of Cr_2O_3/WO_3 at 550 °C and test its photocurrent density. However, the photocurrent density decreased slightly after heating, which was possible due to particles agglomeration (ESI, Fig. S7).

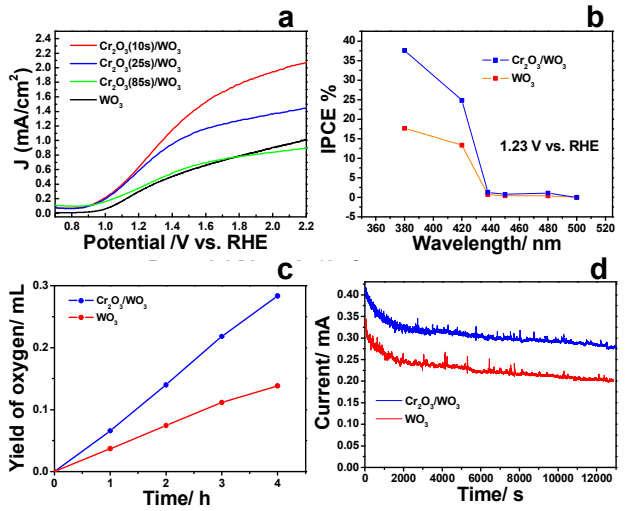

Fig. 4 (a) Linear sweeps voltammogram collected from WO_3 on FTO and Cr_2O_3/WO_3 on FTO after 10, 25 and 85 s electrophoresis deposition, 0.1 M Na_2SO_4 solution, simulated solar illumination (AM 1.5 G, 100 mW cm^{-2}); (b) Incident photon-to-current efficiency (IPCE) of WO_3 on FTO and Cr_2O_3/WO_3 on FTO after 10 s of electrophoresis deposition; (c) Oxygen evolution from WO_3 on FTO and Cr_2O_3/WO_3 on FTO after 10 s of electrophoresis deposition, at 1.0 V vs. RHE under simulated solar illumination (AM 1.5 G, 100 mW cm^{-2}); (d) the time course of photocurrent generation from WO_3 on FTO and Cr_2O_3/WO_3 on FTO after 10 s of electrophoresis deposition during gas evolution, respectively.

The incident photon-to-current efficiency (IPCE) measurements were carried out according to the following equation:[49-52]

$$IPCE = (1240 \times I)/(\lambda \times J_{light}) \times 100 \quad (1)$$

where I is the photocurrent density (mA cm^{-2}), λ the incident light wavelength (nm), and J_{light} the power density of monochromatic light at a specific wavelength (mW cm^{-2}). Compared with pure WO_3, the Cr_2O_3/WO_3 photoanode exhibits a one-fold enhancement in IPCE between 360-430 nm (Fig. 5b, ESI, Fig. S8 enlarges the part from 430 nm to 480 nm). After 430 nm, little enhancement is observed. This suggests the enhancement is mainly due to faster charge separation rather than wider light absorption, which is consistent with the UV-Vis spectra of Cr_2O_3/WO_3 (Fig. 3b). Moreover, the IPCE is measured at different pH in 0.5M H_2SO_4, 0.1M Na_2SO_4 and 1M NaOH (ESI, Fig. S9). Results show that the IPCE values increase with decreasing pH for both WO_3 and Cr_2O_3/WO_3.

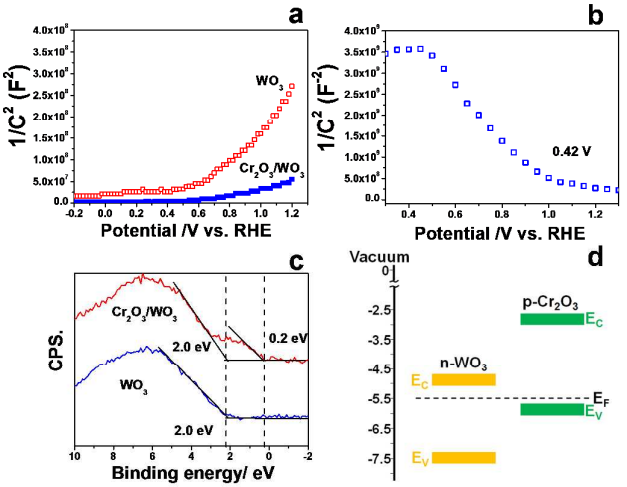

Fig. 5 (a) Mott-Schottky plots of WO_3 and Cr_2O_3/WO_3 at a frequency of 1000 Hz in 0.1 M Na_2SO_4 solution; (b) Mott-Schottky plots of Cr_2O_3; (c) Valence XPS spectra of WO_3 and Cr_2O_3/WO_3. (d) The energy structures of WO_3 and Cr_2O_3, E_F: Femi level.

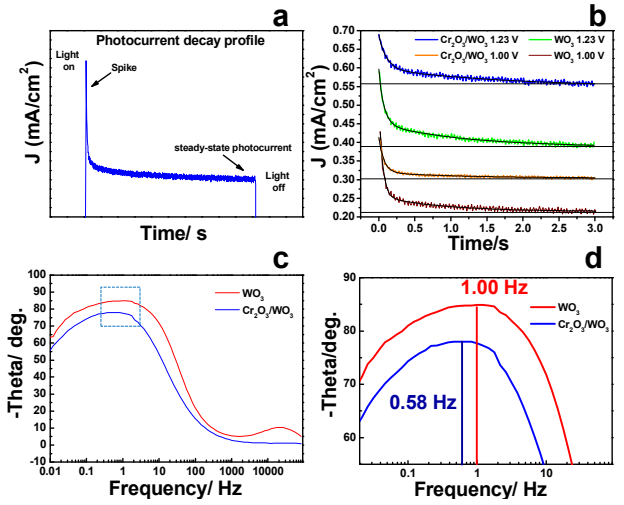

Fig. 6 (a) A typical transient photocurrent decay profile at a constant potential; (b) Transient photocurrent decay profile of WO_3 and Cr_2O_3/WO_3 at 1.0 V and 1.23 V; (c) Bode phase plots of electrochemical impedance spectra of Cr_2O_3 and Cr_2O_3/WO_3 and (d) its zoom-in view of the frame.

The formation of p-n junction between Cr_2O_3 and WO_3 is proved by Mott-Schottky plots and electrochemical measurements (Fig. 5,

ESI, Fig. S10). The Mott-Schottky plots of WO_3, Cr_2O_3 and Cr_2O_3/WO_3 are ploted according to the following equation:[53-55]

$$\frac{1}{C^2} = \frac{2}{\varepsilon \cdot \varepsilon_0 \cdot e_0 \cdot N_D}(E - E_{FB} - \frac{kT}{e_0}) \quad (2)$$

where C is the space charge capacitance, ε and ε_o the permittivity of the electrode and free space, e_0 the elementary charge, E the applied potential, E_{FB} the flat band potential, k the Boltzmann's Constant, and T the temperature.

Table 1. The time constants τ_1 (fast) and τ_2 (slow) for WO_3 and Cr_2O_3/WO_3 calculated from the decay profile of photocurrent, bias: 1.0 V and 1.23 V *vs.* RHE.

	Bias (V)	τ_1(s)	τ_2(s)
WO_3	1.23V	0.071	1.178
WO_3	1.0V	0.050	0.857
Cr_2O_3/WO_3	1.23V	0.104	1.756
Cr_2O_3/WO_3	1.0V	0.070	1.115

In the Mott-Schottky plot, a positive slope often reflects the n-type nature of the semiconductor, while a negative slope reflects the p-type semiconductor.[53, 56, 57] As shown in Fig. 5a, the WO_3, a well-known n-type semiconductor, exhibits a positive slope. While the p-type Cr_2O_3 shows a negative slope (Fig. 5b). The p-type nature of the Cr_2O_3 can also be confirmed by its cathodic photocurrent in CV and transient photocurrent measurement (ESI, Fig. S10). This suggests that a p-n junction is established between Cr_2O_3 and WO_3.

With the formation of p-n junction, the carrier density on the Cr_2O_3/WO_3 photoanode also increases remarkably. As shown in Fig. 5a, the drop of slope in the Mott-Schottky plot indicates the increase of charge carrier.The carrier density of WO_3 is calculated to be 1.31×10^{20} cm^{-3}, while that of Cr_2O_3/WO_3 is 5.87×10^{20} cm^{-3} according to the following equation: [53, 56, 57]

$$N_D = \frac{2}{\varepsilon \cdot \varepsilon_0 \cdot e_0} \cdot \frac{dE}{d\frac{1}{C^2}} = \frac{2}{\varepsilon \cdot \varepsilon_0 \cdot e_0} \cdot \frac{1}{slope} \quad (3)$$

The valence band position of Cr_2O_3 and WO_3 is measured by the edge of maximum energy in valence XPS spectrum (Fig. 5c).[58, 59] The value of WO_3 indicates that its valence band is 2.0 V below the Fermi level, which is consistent with previous report.[59] In the spectrum of Cr_2O_3/WO_3, an additional shoulder with the edge of maximum energy of 0.2 eV appears. It should originate from the Cr_2O_3. The small value of 0.2 eV is consistent with the p-type nature of Cr_2O_3, in which the valence band is very close to the Fermi level. Thus the band structure of Cr_2O_3/WO_3 can be established (Fig. 5d).

An explanation for the enhanced photocurrent density and earlier onset potential of Cr_2O_3/WO_3 photoanode is the suppressed charge recombination inside the p-n junction. To prove this, transient photocurrent measurement is performed to measure the bulk recombination rate of electron/hole pairs.[60] As shown in Fig. 7a, when light is turned on, a relative large transient photocurrent spike is observed, indicating the separation of photoexcited electron/hole pairs.[61] The spike then decays due to the recombination of charge carriers during their migration (holes to the electrolyte and electrons to the external circuit). Finally, a steady-state photocurrent is achieved when charge separation and recombination reach equilibrium. The decay kinetic follows a two order logarithmic equation with two time constants τ_1 (fast) and τ_2 (slow):[62]

$$y = y_0 + A_1 e^{-x/\tau_1} + A_2 e^{-x/\tau_2} \quad (4)$$

Fig. 6b displays the photocurrent transient profile of WO_3 and Cr_2O_3/WO_3 at 1.0 and 1.23 V vs. RHE (original curves see ESI, Fig. S11).The simulated results are shown in Table 1. After formation of p-n junction, the $\tau_1$and τ_2 increase at both 1.0 and 1.23 V vs. RHE, suggesting a lower recombination rate in the p-n junction.

This result is further supported by longer life time of electrons. It is reported that the lifetime of electrons can be evaluated by the maximum frequency peaks (f_{max}) in the Bode phase plots according to $\tau_2 = 1/(2\pi f_{max})$ (Fig. 6c, d, original Nyquist plots see ESI, Fig. S12).[60, 63-65] As shown in Fig. 6d, the f_{max} of WO_3 decreases from 1.00 to 0.58 Hz after the deposition of Cr_2O_3, indicating that the lifetime of electrons increases from 159 to 275 ms. Therefore, the formation of p-n junction can effectively reduce the charge recombination in the photoande. As a result, more electrons could reach the external circuit. This is probably the main reason for the enhancement of photocurrent density and onset potential.

In addition, it is possible that the Cr_2O_3 could also produce photoexcited charge carriers and improve the photocurrent and onset potential. As shown in ESI, Fig. S13 (its IPCE curve), the Cr_2O_3 can generate photoexcited charge carriers before 440 nm, which is consistent with its UV-Vis spectrum. This suggests the photoexcitation of Cr_2O_3 can also contribute to the efficiency of Cr_2O_3/WO_3 photoanode. But its photocurrent density (about 2 uA cm^{-2}) and IPCE value (<0.5 %) are much smaller than those of WO_3 or Cr_2O_3/WO_3, suggesting the contribution from the excitation of Cr_2O_3 is small. Besides, the photovoltage of the p-n junction is also slight larger that than of pure WO_3 photoanode (ESI, Fig. S14). This should be another reason for the negative shift of onset potential.

Another key parameter to evaluate a WO_3 photoanode is the charge-to-chemical faradaic efficiency.[10, 14-22] Faradaic efficiency is defined as the ratio between the charge consumed in the O_2 evolution reaction and the total charge measured during the photocurrent measurement.[1] It displays the utilization efficiency of charges for an electrochemical reaction.

The faradaic efficiency can be evaluated by monitoring the yield of oxygen at 1.0 V vs. RHE (Fig. 4c, V *vs.* RHE (volt) = V *vs.* Ag/AgCl (volt)+[0.059(volt)×pH]+0.236 (volt)). Since this potential is lower than the theoretical threshold of electrolysis water oxidation, the water oxidation is due to photocatalysis. The yield of oxygen from WO_3 is 0.034 mL per hour.

The faradaic efficiency is calculated according to the following equation:[58, 66, 67]

$$\eta_{Faradic} = \frac{4 \times N_{O_2}(mol) \times 96485(C \cdot mol^{-1})}{Q(C)} \quad (5)$$

where $\eta_{Faradaic}$ is the faradaic efficiency for photoelectrochemical water oxidation, N_{O2} is the amount of oxygen, and Q is the total amount of generated charge (Q = photocurrent × time).

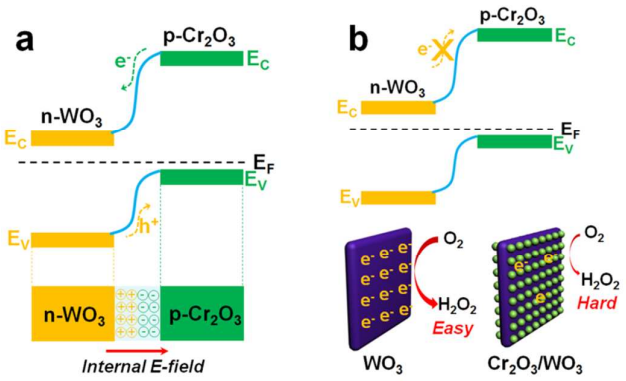

Fig. 7 Schematic diagrams of the mechanism for superior PEC performance of Cr_2O_3/WO_3 photoanode.

Therefore, faradaic efficiency for WO_3 is found to be 73.9%. With Cr_2O_3 decorated, the WO_3 photoanode exhibits higher photocurrent and faster oxygen evolution rate (Fig. 4c). The photocurrent of Cr_2O_3/WO_3 is 1.33 time as high as that of WO_3. Its yield of oxygen increases to 0.058 mL. This is 1.70 times as high as that of WO_3. Accordingly, the faradaic efficiency for oxygen evolution rises to 92.0%. In addition, the hydrogen evolution on the Pt counter electrode is also recorded (ESI, Fig. S15, Fig. S16).

The enhanced faradaic efficiency of Cr_2O_3/WO_3 can be ascribed to the suppression of side reactions induced by the photoexcited electrons (Fig. 7b). In a PEC, the generated oxygen will firstly dissolve in the electrolyte, and then diffuse to the atmosphere for detection. It is reported that the dissolved oxygen is easy to be reduced into hydrogen peroxide by the photoexcited electrons on the surface of photoanodes[68-71] (e.g. on the Fe_2O_3 photoanodes[68,71]). Besides, the hydroxyl intermediates formed during water oxidation will also be reduced by the photoexcited electrons, which will decrease the yield of oxygen.[72, 73] Therefore, the amount of detected oxygen will decrease and lead to a drop in the faradaic efficiency. This phenomenon is more pronounced for n-type WO_3 with electrons as major carrier.[12, 13] However, Cr_2O_3/WO_3 p-n junction can effectively suppress these side reactions induced by photoexcited electrons. As shown in Fig. 7b, the Cr_2O_3 will block the migration of photoexcited electrons from WO_3 to the photoanode/electrolyte interface. This is because the conduction band of Cr_2O_3 is higher than that of WO_3, which is evidenced by XPS valence band (Fig. 5d). Additionally, as the minor carrier, the electron density of the p-type Cr_2O_3 is much lower than that of WO_3. Thus, compared with bare WO_3 photoanode, the total density of photoexcited electrons is lower on the surface of the p-n junction covered with Cr_2O_3 nanocrystals (Fig. 1c, d). This difference will bring a decreased possibility of oxygen and hydroxyl intermediates reduction. As a result, the faradaic efficiency can be enhanced.

Conclusions

In summary, a nanostructured Cr_2O_3/WO_3 p-n junction photoanode is constructed for photoelectrochemical water oxidation. Its band alignment and special morphology result in a low recombination rate and the suppression of side reactions. Therefore, the Cr_2O_3/WO_3 p-n junction photoanode exhibits enhanced PEC activity and a high faradaic efficiency. This work is useful for further understanding the role of p-n junction in photoelectrochemical reaction. Moreover, it will also bring inspiration for fabricating other p-n junction photoanodes with better PEC performance.

Acknowledgements

This work was partially supported by the Shenzhen Basic Research Scheme (JCYJ20120619151417947) and a grant from the Research Grants Council of the Hong Kong Special Administrative Region, China, under Theme-based Research Scheme through Project No. T23-407/13-N. This work was also supported by the National Natural Science Foundation of China (Grant no. 21303118).

Notes and references

a. Key Laboratory of Advanced Ceramics and Machining Technology, Ministry of Education, School of Materials Science and Engineering, Tianjin University, Tianjin 300072, PR China
E-mail: shenzhurui@tju.edu.cn
b. Department of Chemistry, The Chinese University of Hong Kong, Shatin, New Territories, Hong Kong, China & Shenzhen Research Institute, The Chinese University of Hong Kong, Shenzhen, PR China
E-mail: jimyu@cuhk.edu.hk
Electronic Supplementary Information (ESI) available: [It consists of additional SEM, TEM, EDX, optical image, electrochemical data and gas evolution data etc.]. See DOI: 10.1039/x0xx00000x

1 Z. B. Chen, H. N. Dinh and E. Miller, *Photoelectrochemical Water Splitting,* Springer Briefs in Energy, Springer New York Heidelberg Dordrecht London, 2013.
2 A. Fujishima and K. Honda, *Nature,* 1972, **238**, 37.
3 M. Grätzel, *Nature*, 2001, **414**, 338.
4 W. J. Youngblood, S. H. A. Lee, Y. Kobayashi, E. A. Hernandez-Pagan, P. G. Hoertz, T. A. Moore, A. L. Moore, D. Gust, T. E. Mallouk, *J. Am. Chem. Soc.,* 2009, **131**, 926.
5 L. Zhao, X. F. Chen, X. C. Wang, Y. J. Zhang, W. Wei, Y. H. Sun, M. Antonietti and M. M. Titirici, *Adv. Mater.,* 2010, **22**, 3317.
6 C. H. Li, F. Wang and J. C. Yu, *Energy Environ. Sci.*, 2011, **4**, 100.
7 C. Zhen, L. Z. Wang, L. Liu, G. Liu, G. Q. Lu and H. M. Cheng, *Chem. Commun.*, 2013, **49**, 6191.
8 G. Hodes, D. Cahen and J. Manassen, J. *Nature*, 1976, **260**, 312.
9 J. K. Kim, K. Shin, S. M. Cho, T. W. Lee and J. H. Park, *Energy Environ. Sci.*, 2011, **4**, 1465.
10 J. A. Seabold and K.-S. Choi, *Chem. Mater.,* 2011, **23**, 1105.
11 W. J. Li, P. M. Da, Y. Y. Zhang, Y.C. Wang, X. Lin, X. G. Gong and G. F. Zheng, *ACS Nano,* 2014, **8**, *11770*.
12 Y. Xu and M. A. A. Schoonen, *Am. Miner.,* 2000, **85**, 543.

13 R. van de Krol, Y. Q. Liang and J. Schoonman, *J. Mater. Chem.,* 2008, **18**, 2311.
14 Q. Zhao, Z. Yu, W. Yuan and J. Li, *Int. J. Hydrog. Energy,* 2012, **37**, 13249.
15 D. Chandra, K. Saito, T. Yui, M. Yagi, *Angew. Chem. Int. Ed.,* 2013, **52**, 12606.
16 W. Kim, T. Tachikawa, D. Monllor-Satoca, H.-i. Kim,T. Majima and W. Choi, *Energy Environ. Sci.,* 2013, **6**, 3732.
17 Q. X. Mi, A. Zhanaidarova, B. S. Brunschwig, H. B. Gray and N. S. Lewis, *Energy Environ. Sci.,* 2012, **5**, 5694.
18 S. Hilaire, M. J. Suess, N. Kranzlin, K. Bienkowski, R. Solarska, J. Augustynski and M. Niederberger, M. *J. Mater. Chem. A,* 2014, **2**, 20530.
19 Y. Hou, F. Zuo, A. P. Dagg, J. Liu and P. Feng, *Adv. Mater.,* 2014, **26**, 5043.
20 Q. Mi, Y. Ping, Y. Li, B. Cao, B. S. Brunschwig, P. G. Khalifah, G. A. Galli, H. B. Gray and N. S. Lewis, *J. Am. Chem. Soc.,* 2012, **134**, 18318.
21 D. Li, D. Chandra, K. Saito, T. Yui and M. Yagi, *Nanoscale Res. Let.,* 2014, **9**, 542.
22 P. M. Rao, L. L. Cai, C. Liu, I. S. Cho, C. H. Lee, J. M. Weisse, P. D. Yang and X. L. Zheng, *Nano Let.,* 2014, **14**, 1099.
23 H. Dotan, K. Sivula, M. Gratzel, A. Rothschild and S. C. Warren, *Energy Environ. Sci.*, 2011, **4**, 958.
24 F. A. Frame, T. K. Townsend, R. L. Chamousis, E. M. Sabio, T. Dittrich, N. D. Browning and F. E. Osterloh, *J. Am. Chem. Soc.*, 2011, **133**, 7264.
25 S. D. Tilley, M. Cornuz, K. Sivula and M. Gratzel, *Angew. Chem. Int. Ed*, 2010, **49**, 6405.
26 T. A. Abshere and G. L. Richmond, *J. Phys. Chem. B*, 1999, **103**, 7911.
27 T. Zhang, Z. L. Zhu, H. N. Chen, Y. Bai, S. Xiao, X. L. Zheng, Q. Z. Xue and S. H. Yang, *Nanoscale*, 2015, **7**, 2933.
28 W. Z. Li, F. Q. Zhan, J. Li, C. J. Liu, Y. H. Yang, Y. M. Li and Q. Y. Chen, *Electrochim. Acta*, 2015, **160**, 57.
29 D. Chandra, K. Saito, T. Yui and M. Yagi, *Angew. Chem. Int. Ed.*, 2013, **52**, 12606.
30 Y.B. Guo, Q. X. Tang, H. B. Liu, Y. J. Zhang, Y. L. Li, W. P. Hu, S. Wang and D. B. Zhu, *J. Am. Chem. Soc.,* 2008, **130**, 9198.
31 A.D. Mohite, D. E. Perea, S. Singh, S. A. Dayeh, I. H. Campbell, S. T. Picraux and H. Htoon, *Nano Lett.,* 2012, **12**, 1965.
32 F. X. Meng, J. T. Li, S. K. Cushing, M. J. Zhi and N. Q. Wu, *J. Am. Chem. Soc.,* 2013, **135**, 10286.
33 J. Cao, J. Xing, Y. Zhang, H. Tong,Y. Bi, T. Kako, M.Takeguchi and J. Ye, *Langmuir* 2013, **29**, 3116.
34 M. Zhong, T. Hisatomi, Y. Kuang, J. Zhao, M. Liu, A. Iwase, Q. Jia, H. Nishiyama, T. Minegishi, M. Nakabayashi, N. Shibata, R. Niishiro, C. Katayama, H. Shibano, M. Katayama, A. Kudo, T. Yamada and K. Domen, *J. Am. Chem. Soc.*, 2015, **137**, 5053.
35 J. Hou, C. Yang, H. Cheng, S. Jiao, O. Takeda and H. Zhu, *Energy Environ. Sci.*, 2014, **7**, 3758.
36 K. Maeda, K. Teramura, D. L. Lu, N. Saito, Y. Inoue and K. Domen, *Angew. Chem. Int. Ed*, 2006, **45**, 7806.
37 H. Q. Cao, X. Q. Qiu, L. A. Yu, M. J. Zhao and Q. M. Zhu, *Appl. Phys. Lett.*, 2006, 88.
38 L. Xu, Z. Wang, H. Song and L. Chou, *Catal. Comm.*, 2013, **35**, 76.
39 J. L. Bobet, S. Desmoulins-Krawiec, E. Grigorova, F. Cansell and B. Chevalier, *J. Alloy. Compd.*, 2003, **351**, 217.
40 M. Higashi, K. Domen and R. Abe, *Energy Environ. Sci.,* 2011, **4**, 4138.
41 L. Y. Su, L. G. Zhang, J. H. Fang, M. H. Xu and Z. H. Lu, *Solar Energy Materials & Solar Cells,* 1999, **58**, 133.
42 A. M. Mao, J. K. Kim, K. Shin, D. H. Wang, P. J. Yoo, G. Y. Han and J. H. Park, *J. Power. Sour.,* 2012, **210**, 32.
43 X. G. Han, H. Z. He, Q. Kuang, X. Zhou, X. H. Zhang, T. Xu, Z. X. Xie and L. S. Zheng, *J. Phys. Chem. C,* 2009, **113**, 584.
44 M. R. Alenezi, A. S. Alshammari, K. Jayawardena, M. J. Beliatis, S. J. Henley, S. R. P. Silva, *J. Phys. Chem. C,* 2013, **117**, 17850.
45 T. Zhang, K. Zhao, J. Yu, J. Jin, Y. Qi, H. Li, X. Hou and G. Liu, *Nanoscale,* 2013, **5**, 8375.
46 H.Q. Cao, X. Q. Qiu, L. A. Yu, M. J. Zhao and Q. M. Zhu, *Appl. Phys. Lett.,* 2006, **88**. 241112.
47 S. D. Tilley, M. Cornuz,K. Sivula and M. Grätzel, *Angew. Chem. Int. Ed.,* 2010, **49**, 6405.
48 C. Du, X. Yang, M. T. Mayer, H. Hoyt, J. Xie, G. McMahon, G. Bischoping and D. Wang, *Angew. Chem. Int. Ed.,* 2013, **52**, 12692.
49 J. Zhang, J. H. Bang, C. Tang and P. V. Kamat, *ACS Nano* 2010, **4**, 387.
50 Y. Ling, G. Wang, D. A. Wheeler, J. Z. Zhang and Y. Li, *Nano Lett.,* 2011, **11**, 2119.
51 S. Hoang, S. W. Guo, N. T. Hahn, A. J. Bard and C. B. Mullins, *Nano Lett.,* 2012, **12**, 26.
52 M. Xu, P. Da, H. Wu, D. Zhao and G. Zheng, *Nano Lett.,* 2012, **12**, 1503.
53 A. Agarwal, M. N. Vashi and Y. Patel, In *Physics of Semiconductor Devices, Vols 1 and 2*; Kumar, V., Agarwal, S. K., Eds.; Spie-Int Soc Optical Engineering: Bellingham, 1998; Vol. **3316**, p 424.
54 X. Y. Yang, A. Wolcott, G. M. Wang, A. Sobo, R. C. Fitzmorris, F. Qian, J. Z. Zhang and Y. Li, *Nano Lett.,* 2009, **9**, 2331.
55 A. Wolcott, W. A. Smith, T. R. Kuykendall, Y. P. Zhao and J. Z. Zhang, *Small,* 2009, **5**, 104.
56 T. V. Nguyen and O. B. Yang *Catal. Today,* 2003, **87**, 69.
57 C. Baumanis and D. W. Bahnemann, *J. Phys. Chem. C,* 2008, **112**, 19097.
58 N. Li, K. Du, G. Liu, Y. Xie, G. Zhou, J. Zhu, F. Li and H. M. Cheng, *J. Mater. Chem. A,* 2013, **1**, 1536.
59 Y. Hou, F. Zuo, A. Dagg and P. Feng, *Angew. Chem. Int. Ed.,* 2013, **52**, 1248.
60 M. Zhou, J. Bao, Y. Xu, J. Zhang, J. Xie, M. Guan, C. Wang, L. Wen, Y. Lei and Y. Xie, *ACS Nano,* 2014, **8**, 7088.
61 P. Salvador, *J. Phys. Chem.,* 1985, **89**, 3863.
62 D. W. Kim, S. C. Riha, E. J. DeMarco, A. B. F. Martinson, O. K. Farha and J. T. Hupp, *ACS Nano,* 2014, **8**, 12199.
63 C. Cheng, S. K. Karuturi, L. Liu, J. Liu, H. Li, L. T. Su, A. I. Y. Tok and H. J. Fan, *Small,* 2012, **8**, 37.
64 M. Guo, K. Xie, J. Lin, Z. Yong, C. T. Yip, L. Zhou, Y. Wang and H. Huang, *Energy Environ. Sci.,* 2012, **5**, 9881.
65 M. Ye, D. Zheng, M. Lv, C. Chen, C. Lin and Z. Lin, *Adv. Mater.,* 2013, **25**, 3039.
66 C. Liu, J. Y. Tang, H. M. Chen, B. Liu and P. D. Yang, *Nano Lett.,* 2013, **13**, 2989.
67 E. S. Kim, N. Nishimura, G. Magesh, J.Y. Kim, J.-W. Jang, H. Jun, J. Kubota, K. Domen and J. S. Lee, *J. Am. Chem. Soc.,* 2013, **135**, 5375.
68 R. L. Spray, K.J. McDonald and K.-S. Choi, *J. Phys.Chem. C,* 2011, **115**, 3497.
69 R. A. Rincon, J. Masa, S. Mehrpour, F. Tietz and W. Schuhmann, W. *Chem. Commun.,* 2014, **50**, 14760.
70 P. Chen, L.-K. Wang, G. Wang, M.-R. Gao, J. Ge, W.-J. Yuan, Y.-H. Shen, A.-J. Xie and S.-H. Yu, *Energy Environ. Sci.*, 2014, **7**, 4095.
71 F. Fu, T. Jiang, L. Zhang, B. Liu, D. Wang, L. Wang and T. Xie, *J. Mater. Chem. A*, 2014, **2**, 13705.
72 C. Santato, M. Ulmann and J. Augustynski, *J. Phys. Chem. B,* 2001, **105,** 936.
73 Q. X. Mi, A. Zhanaidarova, B. S. Brunschwig, H.B. Gray and N. S. Lewis, *Energy Environ. Sci.,* 2012, **5**, 5694.

TOC

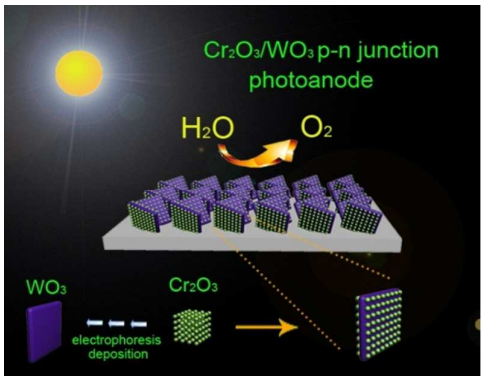

A nanostructured Cr_2O_3/WO_3 p-n junction photoanode has been prepared, which is toward high faradaic efficiency in water oxidation.